PCCP

Check for updates

Oxygen vacancy-enriched Zn₂SnO₄ for aliphatic alcohol sensing and enhanced selectivity towards *n*-butanol

Reshmi Thekke Parayil,[ab] B. Bhagat,[c] Santosh K. Gupta, [ID] *[ab] K. Mukherjee [ID] *[c] and Manoj Mohapatra[ab]

The sensitive detection of toxic flammable volatile organics using low cost efficient sensors is important for ensuring both indoor and outdoor safety. It is essential for chemical sensors to exhibit a significantly stronger response to target analytes compared to equivalent amounts of analogous competing chemicals. In line with this importance, current work evaluated the performance of Zn₂SnO₄, a n-type semiconducting metal oxide, for sensing *n*-butanol in comparison to methanol, ethanol, and propanol vapours. These vapours fall within the category of aliphatic alcohols but vary in characteristics such as molecular weight, vapour pressure, volatility, and diffusivity. In this work we have explored the sensor's performance by adjusting the operating temperature over the range of 225–300 °C while detecting 1000 ppm of each of these vapours. Efforts were made to establish a correlation between the sensor's responses with the interactions of these vapours on the sensor's surface. Prior to assessing the sensing characteristics of the solid-state-route-derived Zn₂SnO₄, its structural characteristics, including phase purity, crystalline structure, bonding patterns, morphology, and defect characteristics, were studied. This comprehensive analysis sheds light on the potential of Zn₂SnO₄ as an effective sensor for detecting *n*-butanol.

ᵃ Radiochemistry Division, Bhabha Atomic Research Centre, Trombay, Mumbai-400085, India. E-mail: santoshg@barc.gov.in

ᵇ Homi Bhabha National Institute, Anushaktinagar, Mumbai-400094, India

ᶜ Department of Chemistry, Pandit Deendayal Energy University, Gandhinagar-382426, Gujarat, India. E-mail: kalisadhanm@yahoo.com

1. Introduction

Semiconducting metal oxide (SMO)-based chemiresistive sensors are popular for the sensitive detection of various gases and volatile organic compounds (VOCs) owing to their simple operation, low cost, high response, durability in harsh environments, and possibilities for miniaturization. Various SMOs, such as ZnO, α-Fe₂O₃, Co₃O₄, SnO₂, and In₂O₃, are already known for the detection of various toxic and inflammable gases.[1–6]

Research activities are underway to modify the existing SMOs by suitable chemical and electronic sensitizers to improve their response characteristics, such as sensitivity, operating temperature, selectivity, and stability. New SMO compositions are also being tested for exploring their sensing characteristics towards various analytes. Understanding critically the role of various parameters that influence the sensing features remains also very important to researchers. Few recent works are highlighted herein to understand the recent trends in SMO-based sensors. In a recent review, Y. Yoon *et al.* reported the factors that could enhance the sensitivity of metal oxide sensors and also discussed the opportunities for metal oxides in developing flexible/wearable sensors.[7] The influence of various parameters (composition, doping, microstructure, crystalline phases, operating temperature, humidity, homo/hetero-junction, interaction type) in modulating the sensing performances of metal oxide chemiresistive sensors were highlighted by S. Das *et al.*[8] Goel *et al.* discussed the different parameters that govern the sensitivity and selectivity of SMO gas sensors and also highlighted the techniques to improve the response of SMO sensors.[9] SMOs in a 1D architecture are attractive as chemiresistive sensors for the detection of various analytes and B. Yang *et al.* reviewed the same.[5] Si *et al.* modified Sr@SnO₂ materials with zeolite (ZSM-5) catalytic materials and reported that temperature modulation was effective for the selective detection of ethanol vapour.[10] For SMO sensors, one of the very fundamental features that influences the receptor and transducer function and alters the overall sensing performance is due to the presence of lattice oxygen vacancies. Al-Hashem *et al.* described in detail the role of oxygen vacancies in modifying the sensing response of metal oxide sensors.[11] The improvement of the gas-sensing performance of a WO₃ sensor by modulating the oxygen vacancies was studied by Yu *et al.*[12] Recently, oxygen-vacancy-enriched SnO₂–RGO hybrids were reported for the room temperature sensing of NO₂.[13] In another recent work, Zhou *et al.* reported H₂ sensing by

modulating the oxygen vacancies in ZnO nanosheets.[14] As reviewed, mostly simple metal oxides and their modified counterparts have been investigated by researchers in sensing studies.

Compared with the aforementioned simple SMOs, binary/ternary metal oxides (with multiple metal ions) have received widespread attention due to their tuneable electrical conductivities and abundant surface active sites.[15–20] In this regard, zinc stannate (Zn_2SnO_4), a ternary, wide-band-gap n-type SMO is attracting the attention of researchers as a promising gas-sensing material. Zinc stannate-based chemiresistive sensors are already being studied for the detection of various gases, including carbon monoxide (CO), nitrogen dioxide (NO_2), methane (CH_4), and volatile organic compounds (VOCs).[21–23] Their promising sensitivity, selectivity to few vapours/gases, and ability to operate in harsh environments make them suitable for gas detection and monitoring. Zn_2SnO_4 has superior electrical conductivity, electron mobility, optical performance, and stability compared to its counterparts ZnO and SnO_2.[24–27] Its band gap varies typically between 3.6–4 eV depending on the reaction conditions, particle size, composition, and defects, which ultimately changes its opto-electronic properties as well as performance, not only for chemiresistive gas sensing but also for other applications, such as in photoconductors, photocatalysis, photoluminescence, photodetectors, lithium-ion batteries, and supercapacitors.[28–31]

The present study explored the possibilities of solid-state-synthesized zinc stannate for the detection of n-butanol, which is a colourless transparent liquid that is extensively used as a solvent, extractant, plasticizer, and reagent in different chemical industries for preparing surfactants, ethylene glycol, butyl ether, rubber products, coating solvents, dibutyl phthalate, *etc.*[32] Prolonged exposure to n-butanol is a health risk as it is corrosive and causes irritation to the human eyes, skin, and respiratory tract. Furthermore, n-butanol is flammable and explosive when mixed with certain organic solvents. Therefore, it would be of great significance to monitor n-butanol in the environment. The properties of n-butanol resemble well modern gasoline and thus the possibility of using this compound as a fuel for combustion engines is being explored by researchers. The presence of 11.5% n-butanol in the air can produce flashes and explosions.[33] In this context, the detection of n-butanol seems crucial for the real-time monitoring of n-butanol in industry and laboratories. Existing butanol sensors have limitations, including cross-sensitivity to other volatile organic compounds, high detection thresholds, susceptibility to environmental factors, calibration needs, and potential drift over time. Further their response times may not meet the demands for rapid detection for many sensors. Ongoing research is seeking to address these issues by enhancing the selectivity, sensitivity, and reliability while reducing the costs and improving the performance. Achieving distinguishably higher responses to the target analytes in particular with respect to their equivalent amount of analogous competing chemicals is important for any chemical sensor.[20,34]

Accordingly, in the present work, the response of Zn_2SnO_4, an n-type SMO, was assessed towards n-butanol with respect to methanol, ethanol, and propanol vapours. These vapours belong to aliphatic alcohols but differ in their molecular weight, vapour pressure, volatility, and diffusivity. The sensing characteristics were measured by varying the operating temperature within the temperature range of 225–300 °C for the detection of 1000 ppm of each of these vapours. An attempt was made to correlate the sensing response by understanding the interactions of the vapours on the sensor surface. Prior to exploring the sensing characteristics of the solid-state-route-derived Zn_2SnO_4, its phase purity, crystalline nature, bonding pattern, morphology, defect characteristics were investigated using XRD, FTIR, Raman spectroscopy, XPS, EPR, TEM, and SAED. The present article thus provides comprehensive insights into the structural features of Zn_2SnO_4 and its potential utilization as an n-butanol sensor.

2. Experimental

2.1. Synthesis

The inverse spinel Zn_2SnO_4 was synthesized by the conventional solid-state-reaction route. The precursors used were ZnO (SPEX Pure, 99.999%) and SnO_2 (SPEX Pure, 99.999%). The required amount of the precursors was weighed and ground in a mortar for complete mixing of the precursors followed by calcining at 900 °C for 15 h in a tubular furnace. Then, it was allowed to cool to room temperature followed by re-grinding. The second stage heating involved sintering at 1200 °C for 15 h. Then, a final grinding was done to obtain the phase-pure compound. The corresponding equation for the solid-state reaction is represented as:

$$2ZnO + SnO_2 \rightarrow Zn_2SnO_4 \qquad (1)$$
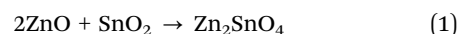
The process flowchart and solid-state-synthesis mechanism is presented in Scheme 1.

2.2. Phase and structural characterization

XRD was carried out using a benchtop Proto X-Ray diffractometer to analyze the phase purity of the synthesized material. The system was equipped with a monochromatic X-ray source as CuKα (1.5405 Å). All the measurements were done at an accelerating voltage of 30 kV and tube current of 20 mA. The XRD patterns were recorded within a 2θ range from 15° to 80° at a scan rate of 2° min^{-1}. FTIR was carried out on a Bruker Alpha FTIR spectrometer in the pellet mode. Raman spectral studies were performed on a micro-Raman spectrometer (STR-300, SEKI Technotron, Japan). A 532 nm CW diode pumped solid-state laser (DPSS, gem 532, laser quantum) was used as an excitation source. The XPS measurements were carried out on a KAlpha plus XPS system (Thermo Fisher Scientific Instruments) to determine the elemental content, chemical state, and the oxygen vacancies. The EPR spectra were recorded on an EMX series Bruker instrument in the X band frequency. The emission spectra were recorded on an Edinburgh fluorescence instrument (FLS 1000), with a xenon lamp as the excitation source. The TEM images and SAED patterns of the material were obtained using a transmission electron microscope (FEI

This journal is © the Owner Societies 2024

Phys. Chem. Chem. Phys., 2024, **26**, 7424–7434 | **7425**
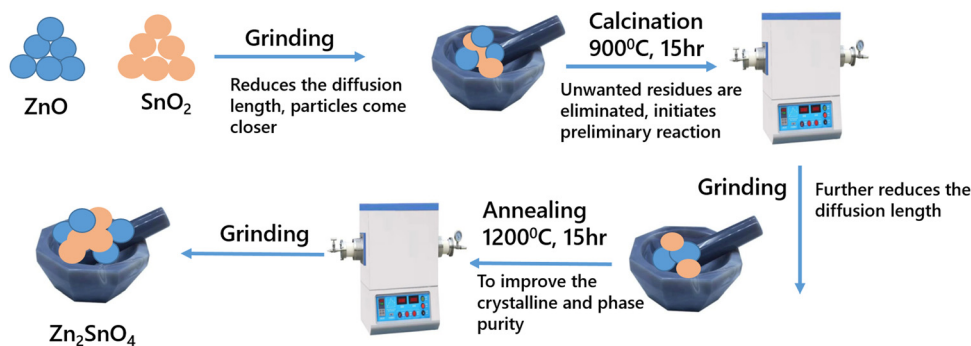
Scheme 1 Solid-state-synthesis flow chart and mechanistic formation of Zn_2SnO_4.

TECNAI G2 F20-ST, FEI) after drop-casting a drop of solution on a carbon-coated copper grid. Energy dispersive X-ray spectroscopy (EDX) analysis was performed using an accelerating voltage of 200 kV.

2.3. VOC sensing studies

In order to measure the sensing properties, the synthesized powder materials were compacted in the form of thin circular discs (10 mm diameter, 1 mm thick). Ag-paste-based parallel strip electrode was prepared on one surface of the electrode. The sample was kept inside the gas-sensing measurement set-up, which included a hot-plate, temperature-controlled probe station, gas injection points, feed through for the electrical connections, and a programmable source meter (Keithley 2450) interfaced with a computer for automatic data acquisition. A schematic representation of the sensing set-up is shown in Scheme 2.

The surface conductance of the sensor was measured by applying fixed DC bias on the electrode. The sensing element was aged at the operating temperature for 2 h in air to ensure a stable electrical contact before starting the sensing measurements. The change in surface conductance of the Zn_2SnO_4 pellet in air (C_a) and in the target gas (C_g) was measured over time by applying voltage on the strip electrodes. The response (S) was estimated as C_a/C_g. The volume of alcohol (V) [99.99% purity] required achieving a specific vapour concentration in ppm inside the test chamber, as obtained using eqn (2).

$$V = \frac{C v_a M}{2.46 \times 10^7 \times D} \quad (2)$$

where C is the required gas concentration (ppm), v_a is the volume of air, which is equal to the volume of test chamber (mL), M is the molecular weight of alcohol (g mol^{-1}), and D is the density of the alcohol (g mL^{-1}). The alcohol sensing properties of the pellet were investigated by injecting the desired concentration of alcohol into the gas chamber.
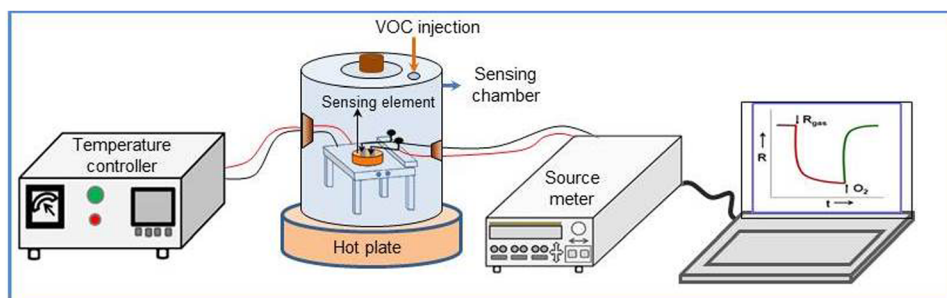
3. Results and discussions

3.1. Phase, vibrational spectroscopy, Raman spectroscopy, and TEM analyses

Fig. 1a presents the XRD pattern of Zn_2SnO_4. The experimentally observed pattern matched with the standard pattern with PDF no. 00-024-1470, suggesting the pure phase formation of highly crystalline Zn_2SnO_4. No other precursor peaks were found in the pattern. The main peaks were observed at 17.7°, 29.1°, 34.2°, 36°, 41.6°, 45.6°, 51.6°, 55.1°, 60.4°, 63.5°, 68.5°, 71.4°, 72.3°, 76°, and 78.9°, corresponding to the (111), (220), (311), (222), (400), (331), (422), (511), (440), (531), (620), (533), (622), (444), and (711) planes. The observed diffraction peaks corresponded to the cubic inverse spinel structure of Zn_2SnO_4.[35] The crystallite size was determined using the Debye–Scherrer formula.

$$t = \frac{k\lambda}{\sqrt{(B_S^2 - B_M^2)}\cos\theta} \quad (3)$$

where t represents the crystallite size; k is Scherrer's constant (0.9); λ is the wavelength of the CuKα line (1.5406 Å); θ is the angle corresponding to the Bragg reflection, which is used for calculating the full width at half maximum (FWHM); and B_S and

Scheme 2 Representation of the gas sensing set-up.

7426 | *Phys. Chem. Chem. Phys.*, 2024, **26**, 7424–7434

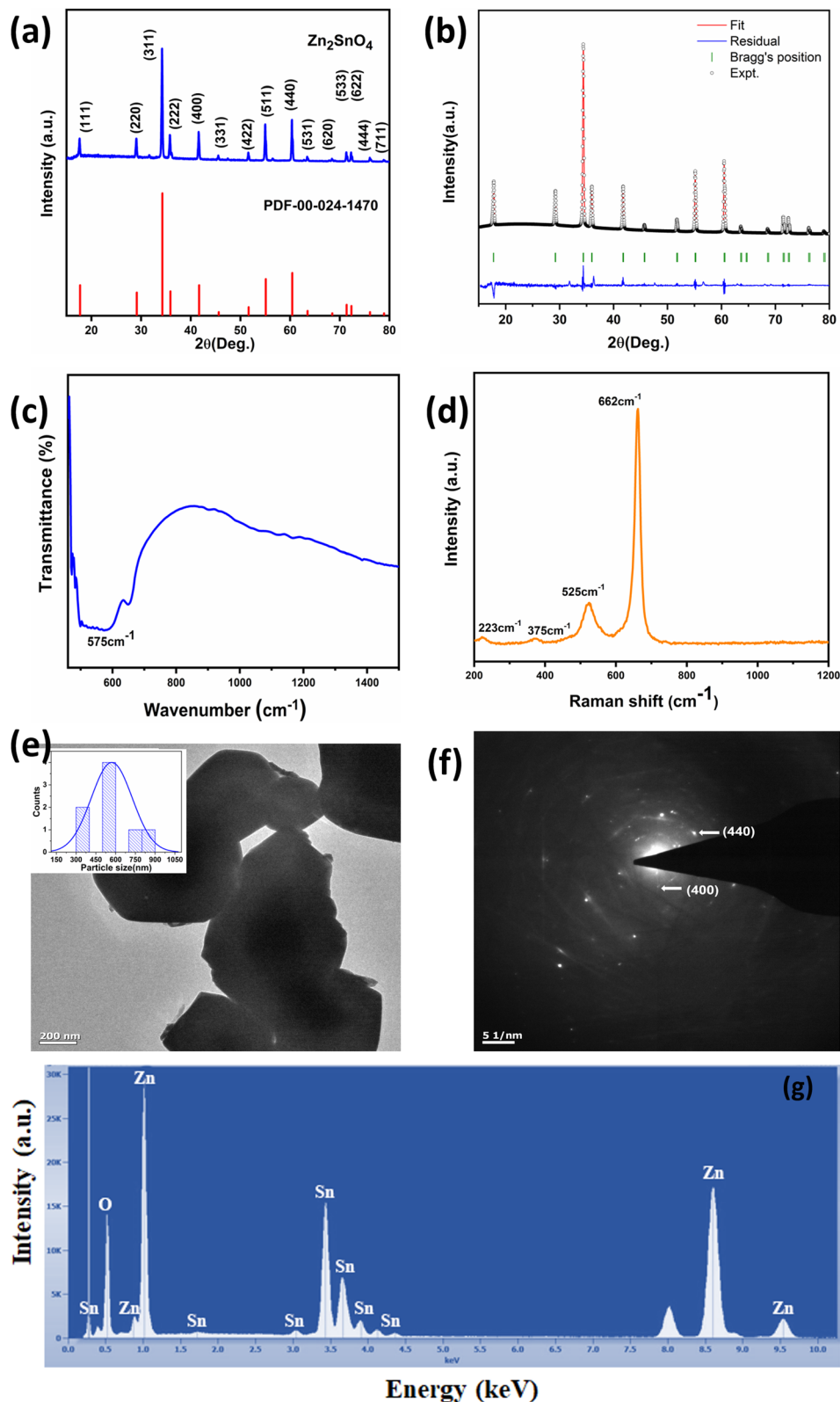This journal is © the Owner Societies 2024

Fig. 1 (a) Powder XRD pattern, (b) Rietveld pattern, (c) FTIR spectrum, (d) Raman spectrum, (e) TEM image, (f) SAED pattern, and (g) EDX spectrum of Zn_2SnO_4.

B_M are the FWHM values (in radian) of the selected diffraction peaks of the sample and reference (LaB_6). The FWHM was calculated by fitting the curve to a pseudo-Voigt function. The instrumental broadening was considered by subtracting the

This journal is © the Owner Societies 2024

Phys. Chem. Chem. Phys., 2024, **26**, 7424–7434 | **7427**

contribution from the reference LaB_6. The average crystallite size was estimated as 39.03 nm. Fig. 1b shows the Rietveld refinement plot of Zn_2SnO_4. The value of the lattice constant (a) was obtained as 8.65139 Å, which matches with the literature values,[36] whereas the cell volume was 647.5 Å^3.

Fig. 1c presents the FTIR spectrum of Zn_2SnO_4, which was recorded in the range from 480 to 1500 cm^{-1}. The sample was prepared in the form of a pellet using KBr. The spectrum displayed a broad peak at 575 cm^{-1}, corresponding to vibration of the Sn–O–Zn bond in Zn_2SnO_4,[25] and a shoulder peak at 650 cm^{-1}, corresponding to vibration of the Sn–O bond.[37]

According to Group theory, there are 5 Raman active modes for bulk Zn_2SnO_4. Theoretically, the peaks are at 143, 227, 377, 532, and 667 cm^{-1}, corresponds to the $T_{2g}(1)$, E_g, $T_{2g}(2)$, $T_{2g}(3)$, and A_{1g} symmetries. As can be seen in Fig. 1d, the Raman peaks here were at 223, 375, 525, and 662 cm^{-1}, which were in agreement with the theoretical values.[38] The peak at 662 cm^{-1} corresponded to the stretching vibration of the short M–O bond in the MO_6 octahedron. The peak at 525 cm^{-1} corresponded to the internal vibration of the oxygen tetrahedron.[39,40] Fig. 1e and f correspond to the TEM and SAED pattern of the material. TEM suggested that the particles had sizes >300 nm. From the SAED pattern, sharp diffractions spots could be observed, which suggest that the synthesized material possess good crystallinity. The patterns were indexed to the (440) and (400) crystal planes, respectively.[35] Fig. 1g presents the EDX spectrum of Zn_2SnO_4 for confirming the elemental composition of the prepared material, which confirmed the material was pure with no impurities.

In order to confirm the surface composition and valence state, XPS was performed. The survey scan of Zn_2SnO_4 is shown in Fig. 2a. From the survey spectra the presence of Zn, Sn, and O was confirmed. The Zn 2p convoluted spectrum is shown in Fig. 2b, where 2 peaks with binding energy values of 1022 and 1045 eV could be observed, corresponding to Zn 2p$_{3/2}$ and Zn 2p$_{1/2}$, respectively. The spin orbit splitting value of 23 eV confirmed that Zn existed in the Zn^{2+} valence state. Fig. 2c presents the Sn 3d convoluted spectrum, with 2 symmetric peaks at 495 and 486.6 eV, corresponding to Sn 3d$_{3/2}$ and 3d$_{5/2}$, respectively, while the peak spacing of 8.4 eV confirmed the Sn^{4+} valence state.[41] Fig. 2d presents the O 1s spectrum, which was deconvoluted into 3 peaks with binding energy values of 530, 531, and 532 eV. The first peak corresponded to the lattice oxygen (M–O), the second peak to the oxygen vacancies, and the third peak to the chemisorbed oxygen.[42] Thus the XPS analysis confirmed the purity of the prepared material.

Fig. 2e presents the EPR spectrum of Zn_2SnO_4. The spectrum consisted of a resonance signal at $g = 1.98$, corresponding to the electrons trapped in the oxygen vacancies.[43,44] The emission spectrum shown in Fig. 2f resulted from excitation at 320 nm, in which a broad emission could be observed ranging from 500 to 1000 nm, which was mainly contributed by the defect levels between the band gap. The broad emission was composed of green, orange, and red emission, which was mainly due to the presence of oxygen vacancies, and the interaction of oxygen vacancies, oxygen interstitials, Sn interstitials, interstitial Zn, and Sn vacancies respectively. The broad peak could be deconvoluted into 3 peaks with maxima at 562, 639, and 744 nm. The emission spectra are shown in the inset of Fig. 2f. Hu *et al.*[45] reported a broad orange red emission for Zn_2SnO_4 nanowires, which was due to the interaction of oxygen and tin vacancies and/or interstitial oxygen (orange). The other emission (in the red region) was due to the variation in the Zn/Sn stoichiometry and the disorder in the inverse spinel structure.[46] Also Zn_2SnO_4 micro prisms synthesized by Zhao *et al.* exhibited an asymmetric broad band emission around 606 nm and 740 nm, which was
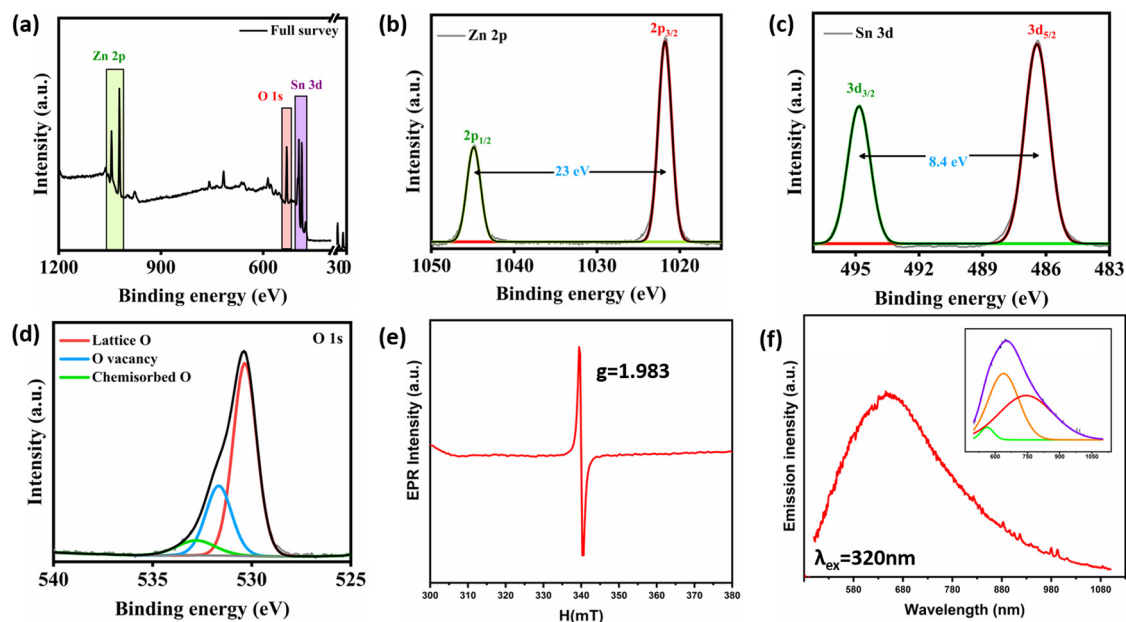

Fig. 2 (a) XPS survey scan, core level spectra of: (b) Zn 2p, (c) Sn 3d, (d) O 1s; (e) EPR spectrum; and (f) photoluminescence spectrum of Zn_2SnO_4.

7428 | *Phys. Chem. Chem. Phys.*, 2024, **26**, 7424–7434

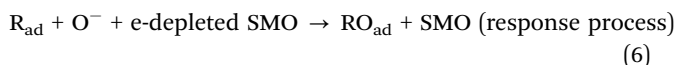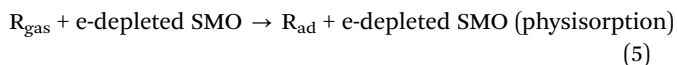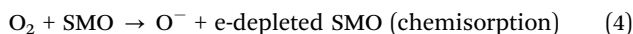This journal is © the Owner Societies 2024

due to the interactions between the oxygen vacancies and the interfacial tin and/or zinc defects.[47]

3.2. VOC-sensing studies

The prepared Zn_2SnO_4 sensing element showed n-type sensing characteristics, *i.e.* the electrical conductance of the sensor increases in the presence of reducing vapours (*e.g.* methanol, ethanol, propanol, butanol *etc.*). The mechanism for chemiresistive sensing by a typical n-type SMO for the detection of reducing vapors, *e.g.* ethanol, is schematically presented in Fig. 3. As shown in Fig. 3(a), when the semiconducting metal oxide (SMO) sensor is kept at elevated temperature, oxygen is chemically adsorbed on its surface. Such chemi-adsorption of oxygen makes the particles electronically depleted. Particles having enriched oxygen vacancies deplete more than the normal metal oxide particles due to the chemisorption of a higher amount of oxygen. The chemisorption of oxygen on metal oxide followed by the formation of an electron-depleted layer eventually increases the potential barrier (qVs) for interparticle charge transportation, leading to the increase in resistance of the sample.

Upon exposure to reducing vapours, the chemi-adsorbed oxygen ions react with the vapours and the released electrons come back to the conduction bands of the SMO particles. As a result, the resistance of n-type sensing materials decreases upon exposure to reducing gases. Fig. 3(b) shows the formation and lowering of the potential barriers when oxygen and reducing gases were exposed respectively on the SMO surface. The respective change in the sensor resistances is shown in Fig. 3(c). The sequential phenomenon of the sensing process over SMO can further be described using the following reactions:

$$O_2 + SMO \rightarrow O^- + \text{e-depleted SMO (chemisorption)} \quad (4)$$

$$R_{gas} + \text{e-depleted SMO} \rightarrow R_{ad} + \text{e-depleted SMO (physisorption)} \quad (5)$$

$$R_{ad} + O^- + \text{e-depleted SMO} \rightarrow RO_{ad} + SMO \text{ (response process)} \quad (6)$$

$$RO_{ad} + SMO \rightarrow RO_{gas} + SMO \text{ (recovery process)} \quad (7)$$

Eqn (4) represents the chemisorption of atmospheric oxygen on the SMO surface leading to the formation of the electron-depleted SMO (e-depleted SMO). The reducing gas (R_{gas}) when exposed on the e-depleted SMO becomes physisorbed (eqn (5)). The physisorbed reducing gas (R_{ad}) is then oxidized by chemisorbed oxygen forming RO_{ad} (eqn (6)). The oxidation of the physisorbed reducing gas by the chemisorbed oxygen is considered to be the rate-determining step for the response process. The adsorbed oxidized product is then desorbed as RO_{gas}, recovering the e-depleted SMO in the presence of air during the recovery process (eqn (7)). The response and recovery for the detection of reducing gases over the SMO surface can thus be considered as the catalytic oxidation of reducing vapours at elevated temperature, where SMO acts as the catalyst. The overall reaction thus can be expressed as follows:

$$SMO \xrightarrow{+T/+O_2} \text{e-depleted SMO} + O^- + R_{gas} \rightarrow$$
$$R_{gas} + \text{e-depleted SMO} \xrightarrow{-T/-O_2} SMO \quad (8)$$
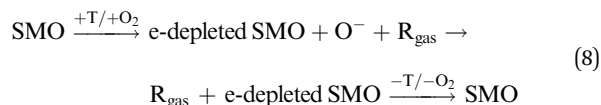
The chemical composition, defects, size, and band structure of metal oxides influence the chemiresistive sensing characteristics. Defects or vacancies in the form of oxygen vacancies typically arise during the formation of metal oxides, and they exert a significant influence on the sensing properties of these materials. The role of oxygen vacancies for improving the gas sensing by metal oxides has also been reported elsewhere.[11,12,48]

The formation of oxygen vacancies within a metal oxide crystal lattice can be represented by the following reaction:

$$O_O^\times \leftrightarrow \tfrac{1}{2}O_2(g) \uparrow + V_O^{\bullet\bullet} + 2e' \quad (9)$$
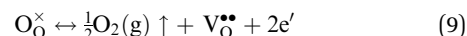
where $O_O^\times$ is the oxygen atom lost from the lattice as oxygen gas $[\tfrac{1}{2}O_2(g)]$, creating positively charged oxygen vacancies ($V_O^{\bullet\bullet}$) in the lattice. To maintain the charge neutrality, each $V_O^{\bullet\bullet}$ traps electrons (e'), which act as donor levels within the band gap.

For SMO sensors, the presence of oxygen vacancies modulates both the receptor and transducer functions, which control, respectively, the interaction of the target analyte on the sensing surface and the transportation of the generated
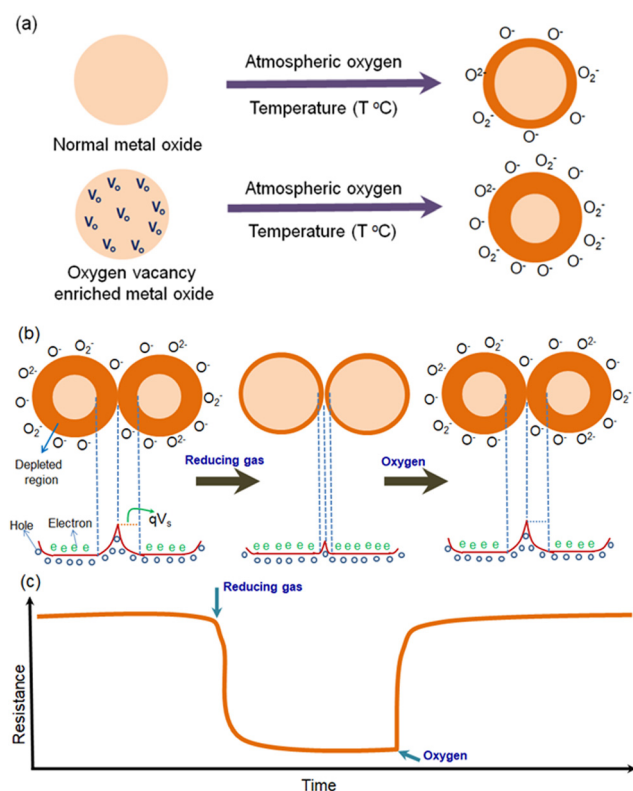

Fig. 3 Schematic showing (a) the chemisorption of oxygen on normal and oxygen-vacancy-enriched semiconducting metal oxide particles and the formation of an electron-depleted layer. (b) Change in the depleted-layer-induced potential barrier in the SMO grains due to the exposure to reducing gas and air. (c) Change in the resistance transients of the SMO sensor when going back and forth between air and reducing vapours.

This journal is © the Owner Societies 2024

Phys. Chem. Chem. Phys., 2024, **26**, 7424–7434 | **7429**

electronic signal within the sensor. The oxygen vacancy sites $(V_O^{\bullet\bullet})$ in SMO enhance the chemisorption of oxygen on the sensing surface kept at an elevated temperature. The chemisorbed oxygens help improving the receptor function by oxidizing more of the target gas. The electrons released in the defect state at the conductance band minimum (CBM) act as donor sites and help improving the transduction of the electronic signal within the sensor.

The role of oxygen vacancies in modulating the sensing performance of SMO can further be explained using the width of the electron-depleted layer that is formed due to the chemisorption of oxygen on the SMO surface at elevated temperature. The width (L_D) of the electron-depleted layer can be expressed according to the following relations:

$$L_D = (\varepsilon_0 kT/n_0 e^2)^{1/2} \tag{10}$$

where ε_0 is the static dielectric constant of the metal oxide, n_0 is the remaining donor concentration, e is the carrier charge, k is the Boltzmann constant, and T is the absolute temperature.

At a fixed temperature, the change of L_D will be more prominent for oxygen-vacancy-enriched metal oxide, leading to a superior response of the sensor. The presence of oxygen vacancies in Zn_2SnO_4 was already confirmed by the EPR and XPS analyses, as shown in Fig. 2. The aforementioned influence of oxygen vacancies is also applicable for alcohol sensing by the n-type Zn_2SnO_4.

Fig. 4 shows the conductance transients of the Zn_2SnO_4 sensing element at (a) 225 °C, (b) 250 °C, (c) 275 °C, and (d) 300 °C for the detection of 1000 ppm methanol (MeOH), ethanol

(EtOH), *n*-propanol (PrOH), and *n*-butanol (BtOH). At each temperature, two conductance transients were recorded for each of the target vapours. At 225 °C, the conductance transients were a bit noisier and the base resistance did not recover fully when the test vapours and oxygen flowed back and forth on the sensing element. However, at higher temperature (250–300 °C), the recorded transients were distinct for each of the test vapours. It was notable that for a fixed test vapour, the conductance transients were identical, which demonstrated that the sensor could identify the target vapour and produce a characteristic chemiresistive sensing signal. Comparing the conductance transients, it seemed that the sensor showed the maximum change in conductance in the presence of butanol vapour.

The variation of the estimated response with the sensor operating temperature is shown in Fig. 5. As displayed in the figure, the response of the sensor increased with the rise in the operating temperature. This can be explained by the concept of the temperature-dependent chemisorption of oxygen on the metal oxide surface. The chemisorption of oxygen on the metal oxide surface increased with the rise in operating temperature, resulting in an enhanced opportunity to oxidize the target reducing vapours, and thus the response of the sensor also increased with the operating temperature. At lower operating temperature (225 °C and 250 °C), the selectivity towards butanol was not profound compared to the other studied vapours. However, at higher temperature the response of the sensor towards butanol vapour was noticeably higher.

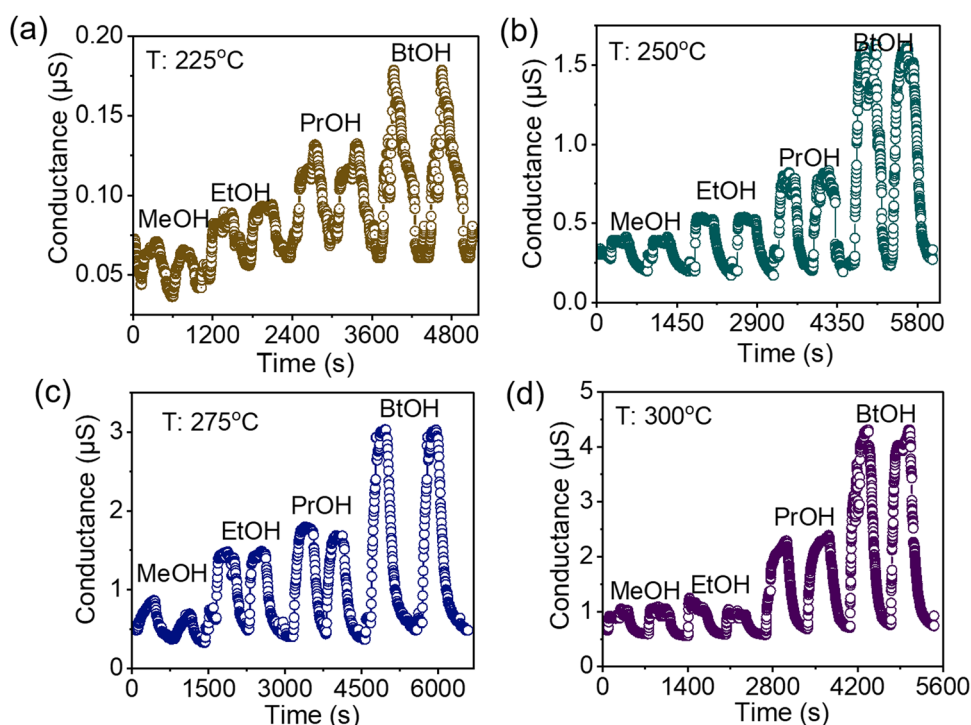The response of the SMO chemiresistive sensor towards gases and vapours is a complicated process[8,49,50] that is

Fig. 4 Conductance transients of Zn_2SnO_4 for sensing 1000 ppm methanol, ethanol, propanol, and butanol at (a) 225 °C, (b) 250 °C, (c) 275 °C, and (d) 300 °C.

7430 | *Phys. Chem. Chem. Phys.*, 2024, **26**, 7424–7434
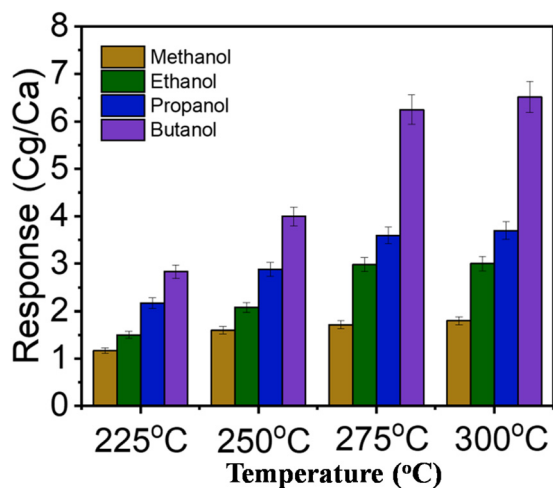
This journal is © the Owner Societies 2024

Fig. 5 Temperature-dependent response of Zn_2SnO_4 for the detection of alcohol vapours.

governed by two physical functions, namely the receptor and transducer functions, which are influenced by the characteristics of sensing materials (*e.g.* chemical composition, conductivity, bandgap, surface area, porous nature, morphology), sensor architecture (*e.g.* thin film, thick film, powder compacted disk), physical and chemical properties of vapours (*e.g.* mass, diffusivity, boiling point, shape and size of molecules, oxidation probability), and also on the measurement conditions (*e.g.* temperature, vapour concentration). The entangled effect of all these parameters influences the sensing characteristics, and the critical comparison of the individual sensing responses varying with temperature becomes difficult. However, at a particular temperature, for a fixed sensing element, the sensor transients are mainly the reflection of the adsorption, diffusion, and interaction of the respective vapours with the sensor surface. As envisaged from the table, at a fixed studied operating temperature (225/250/275/300 °C), the sensing response (S) followed the trend: $S_{Butanol} > S_{Propanol} > S_{Ethanol} > S_{Methanol}$. In order to understand the sensing responses of the vapours, we took a few physical (molecular weight, diffusivity in air, density, boiling point) and chemical (chemical structure as well as adsorption and oxidation probability) properties into consideration (as summarized in Table 1).

The higher molar mass and boiling point of *n*-butanol led to its low vapour pressure and lower diffusion in air (within the sensing chamber) resulting in the superior adsorption on the sensing surface than the other studied alcohol vapours.

The trends for the polarity of the –O–H bond is methanol > ethanol > *n*-propanol > *n*-butanol, with the oxidation probability in the same order.

The selectivity towards butanol compared to other vapours was not profound at lower temperature (225/250 °C) due to its higher adsorption but lower oxidation probability. However, the higher oxidation of butanol at increased operating temperature improved its selectivity. In order to understand and correlate the vapour–solid interactions with the chemiresistive sensing signal, the response transients of the sensors for the detection of all the studied vapours were recorded at 275 °C and 300 °C, and are compared in Fig. 6a and b, respectively. The figures clearly show that at 275 °C and 300 °C, the sensor response towards butanol was significantly higher than for the other vapours. The response times for the detection of the vapours were also less than <60 s. The alcohol, in particular butanol, sensing performances of the prepared Zn_2SnO_4 were further compared with the already reported SMO chemiresistive sensors, and the results are summarized in Table 2. As envisaged from the table, the simple metal oxide and their modified counterparts are known for the sensing of alcohol vapours, including butanol. However, Zn_2SnO_4-based materials are not very frequently reported for sensing alcohol with a higher response towards butanol. The operative temperature of the present Zn_2SnO_4 sensor was also comparable to the already reported sensors. Further research studies thus need to explore suitable modifications of primitive Zn_2SnO_4 for the detection of even lower concentrations of butanol at low operating temperatures.

4. Conclusions

The present work evaluated the Zn_2SnO_4 sensor performance with adjusting the operating temperature in the range of 225–300 °C for different aliphatic alcohols with 1000 ppm concentration. The synthesized material was well characterized by XRD, FTIR, Raman spectroscopy, EDX, TEM, and XPS. The formation of phase-pure Zn_2SnO_4 with good crystallinity was confirmed through the XRD in conjunction with FTIR and Raman spectra analyses. The defect characterizations as well as photophysical properties analysis were carried out using EPR and photoluminescence measurements, respectively. The XPS, EPR, and PL results in combination suggested the presence of oxygen vacancies in the synthesized materials. The role of oxygen vacancies in modulation of the sensing performances of semiconducting metal oxide sensors was investigated and

Table 1   Properties of the studied alcohol vapours

Analyte	Molar mass (g mole^{-1})	Mean molecular radius (Å)	Boiling point (°C)	Vapour pressure (kPa) at 25 °C	Diffusion in air coefficient (cm^2 s^{-1}) at 25 °C
Methanol (CH_3–OH)	32.04	4.11	65	11.9	0.177
Ethanol (CH_3–CH_2–OH)	46.07	4.64	78	5.95	0.126
n-Propanol (CH_3–CH_2–CH_2–OH)	60.1	5.10	97	2	0.089
n-Butanol (CH_3–CH_2–CH_2–CH_2–OH)	74.12	5.52	117	0.9	0.053

This journal is © the Owner Societies 2024

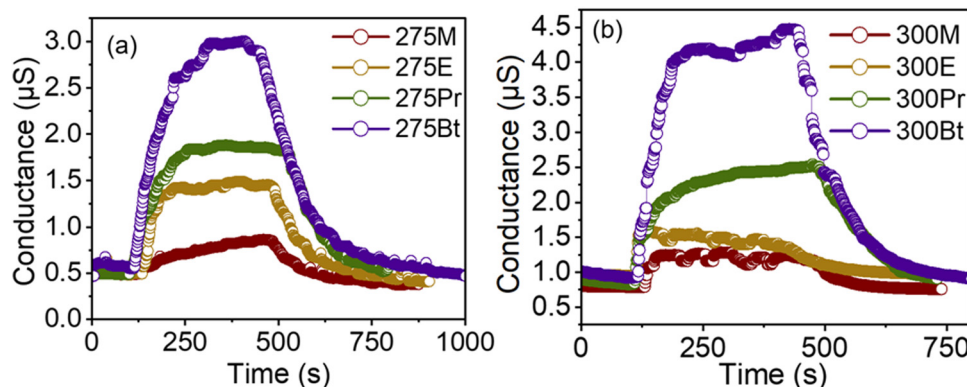*Phys. Chem. Chem. Phys.,* 2024, **26**, 7424–7434 | **7431**

Fig. 6 Comparison among the sensing responses towards methanol, ethanol, propanol, and butanol vapours at (a) 275 °C and (b) 300 °C.

Table 2 Comparative study of the Zn_2SnO_4 sensor in this work with previously reported alcohol sensors

S. no.	Material	Targeted analyte/s	Operating temperature	Minimum detection	Ref.
1.	Al_2O_3/ZnO	Propanol, n-butanol, ethanol, acetone, hydrogen, and ammonia	350 °C	100 ppm	51
2.	In_2O_3/Pt nanoparticles and Ag nanowires	Ethanol	125 °C	200 ppm	52
3.	Pd-doped SnO_2 nanoparticles	Methanol, ethanol, acetone, or hydrogen	—	1000 ppm	53
4.	CeO_x-doped SnO_2 nanoparticles	C_3H_6O, CH_4, H_2, NO_2, H_2S, and H_2O	350 °C	200 ppm	54
5.	SnO_2	Ethanol, isopropyl alcohol, acetone, and ammonia	90 °C	800 ppm	55
6.	Pd–SnO_2	Methanol and ethanol	200–400 °C	—	56
7.	Lanthanum-loaded indium tin oxide (ITO)	Ethanol	300 °C	100 ppm	57
8.	Soda-lime glass slide was decorated with palladium nanoparticles	Acetone, benzene, ethanol, and toluene	300–500 °C	30 ppm	58
9.	SnS–ZnS composite	Ethanol	27 °C	100 ppb	59
10.	ZnO nano-flowers	Methanol and ethanol	250 °C	700 ppm	60
11.	CuO-decorated Fe_2O_3 nanoflakes	Ethanol	250 °C	100 ppm	61
12.	Sm_2O_3/ZnO/$SmFeO_3$ microspheres	Methanol	195 °C	5 ppm	62
13.	MoS_2/TiO_2 composite	Methanol ethanol	300 °C	5 ppm	63
14.	Pd-doped CeO_2 nanofibers	Hydrogen, carbon monoxide, ammonia, ethanol, methanol, and benzene.	200 °C	100 ppm	64
15.	Coating Au nanoclusters onto ZnO and Co_3O_4 sensors	Ethanol, benzene, toluene, and p-xylene	450 °C	100 ppm	65
16.	Pt-modified WO_3/p-Si film with Al	Methanol	25 °C	—	66
17.	Zn doped NiO samples	Methanol	260 °C	100 ppm	67
18.	$Co_xLaFe_{1-x}O_3$, x = 0.00, 0.01, 0.05, and 0.10	n-Butanol	—	10 ppm	68
19.	ZnO–In_2O_3 nanocomposites	n-Butanol	220 °C	50 ppm	69
20.	Palladium-doped SnO_2	n-Butanol		100 ppm	70
21.	ZnO@TiO_2	n-Butanol	200 °C	133	71
22.	CdO/ZnO nanocomposites	n-Butanol	300 °C		72
23.	$ZnSnO_3$ hollow spheres	n-Butanol	200 °C	300 ppm	73
24.	$ZnFe_2O_4$ macroporous spheres	n-Butanol	250 °C	100 ppm	74
25.	Zn_2SnO_4	n-Butanol	225–300 °C	100 ppm	Present work

discussed. The sensing performance for different reducing vapours (methanol, ethanol, propanol, and butanol) was studied in the temperature range of 225–300 °C. The response of the sensor was maximum at 300 °C. Among the four aliphatic alcohols, n-butanol had a superior sensing response due to its higher molar mass and boiling point, which led to its low vapour pressure and lower diffusion in air. The estimated response of the sensor was 4.5 for the detection of 1000 ppm butanol at 300 °C. The response time of the sensor for the detection of 1000 ppm butanol at 300 °C was <60 s. The response and recovery for the detection of reducing vapours

over the Zn_2SnO_4 surface could thus be considered as due to the catalytic oxidation of reducing vapours at elevated temperature where Zn_2SnO_4 acted as a catalyst. This study reveals the potential of Zn_2SnO_4 as an effective sensor for detecting n-butanol. This study reveals that oxygen-vacancy-enriched Zn_2SnO_4 could be an effective sensor for selectively detecting n-butanol. However, the particle size of Zn_2SnO_4 was found to be a little bigger (400–800 nm), which should be reduced further to improve the response of the sensor. The primitive Zn_2SnO_4 may also be modified with suitable chemical/electronic sensitizers to make it operative at lower temperature.

Conflicts of interest

There are no conflicts to declare.

Acknowledgements

References

1 P. M. Bulemo and J. Y. Cheong, *ACS Appl. Nano Mater.*, 2023, **6**, 1027–1049.

2 P. Das, B. Mondal and K. Mukherjee, *J. Phys. Chem. C*, 2017, **121**, 1146–1152.

3 M. Khatib and H. Haick, *ACS Nano*, 2022, **16**, 7080–7115.

4 S. Tyagi, M. Chaudhary, A. K. Ambedkar, K. Sharma, Y. K. Gautam and B. P. Singh, *Sens. Diagn.*, 2022, **1**, 106–129.

5 B. Yang, N. V. Myung and T.-T. Tran, *Adv. Electron. Mater.*, 2021, **7**, 2100271.

6 S. K. Gupta, S. Mohan, M. Valdez, K. Lozano and Y. Mao, *Mater. Res. Bull.*, 2021, **142**, 111419.

7 Y. Yoon, P. L. Truong, D. Lee and S. H. Ko, *ACS Nanosci. Au*, 2022, **2**, 64–92.

8 S. Das, S. Mojumder, D. Saha and M. Pal, *Sens. Actuators, B*, 2022, **352**, 131066.

9 N. Goel, K. Kunal, A. Kushwaha and M. Kumar, *Eng. Rep.*, 2023, **5**, e12604.

10 R. Si, Y. Xu, C. Shen, H. Jiang, M. Lei, X. Guo, S. Xie, S. Gao and S. Zhang, *ACS Sens.*, 2024, DOI: **10.1021/acssensors.3c01831**.

11 M. Al-Hashem, S. Akbar and P. Morris, *Sens. Actuators, B*, 2019, **301**, 126845.

12 W. Yu, Z. Shen, F. Peng, Y. Lu, M. Ge, X. Fu, Y. Sun, X. Chen and N. Dai, *RSC Adv.*, 2019, **9**, 7723–7728.

13 Y. Zhang, Y. Xing, Z. Yang, L. Zhao, C. Xin, Z. Wei, T. Fei, S. Liu and T. Zhang, *Mater. Today Commun.*, 2024, **38**, 108090.

14 S. Zhou, W. Yan, M. Ling and C. Liang, *Inorg. Chem. Front.*, 2023, **10**, 3255–3262.

15 M. Karmakar, B. Mondal, M. Pal and K. Mukherjee, *Sens. Actuators, B*, 2014, **190**, 627–633.

16 K. Mukherjee and S. B. Majumder, *Int. J. Hydrogen Energy*, 2014, **39**, 1185–1191.

17 A. Šutka and K. A. Gross, *Sens. Actuators, B*, 2016, **222**, 95–105.

18 R. T. Parayil, S. K. Gupta, R. Rohilla, J. Prakash, K. Sudarshan and M. Mohapatra, *ACS Appl. Electron. Mater.*, 2023, **5**, 5151–5163.

19 R. T. Parayil, G. D. Patra, B. Modak, K. Sudarshan, M. Sonawane, S. Sen and S. K. Gupta, *ACS Appl. Opt. Mater.*, 2023, **1**, 179–192.

20 L. Mao, S. Mohan, S. K. Gupta and Y. Mao, *Mater. Chem. Phys.*, 2022, **278**, 125643.

21 N. Joshi, H. Long, P. Naik, A. Kumar, V. R. Mastelaro, O. N. Oliveira, A. Zettl and L. Lin, *New J. Chem.*, 2022, **46**, 17967–17976.

22 S. Ma, L. Shen, S. Ma, J. Wen and J. Xu, *Coord. Chem. Rev.*, 2023, **490**, 215217.

23 L. Wang, T. Zhou, R. Zhang, Z. Lou, J. Deng and T. Zhang, *Sens. Actuators, B*, 2016, **227**, 448–455.

24 A. A. Bhat, I. Assadullah, A. Farooq, K. A. Malik, J. H. Malik, R. Tomar, I. Islam, A. M. Ali and S. A. Khandy, *Mater. Chem. Phys.*, 2023, **306**, 127993.

25 P. Pratim Das, A. Roy, S. Das and P. S. Devi, *Phys. Chem. Chem. Phys.*, 2016, **18**, 1429–1438.

26 M. Zhang, X. Cui, Y. Wang, B. Wang, M. Ye, W. Wang, C. Ma and Z. Lin, *Nano Energy*, 2020, **71**, 104620.

27 Y. Zhang, X. Xin, H. Sun, Q. Liu, J. Zhang, G. Li, J. Gao, H. Lu and C. Wang, *J. Alloys Compd.*, 2021, **854**, 157311.

28 S. K. Gupta, K. Sudarshan, D. Chandrashekhar, A. Balhara and M. Mohapatra, *J. Lumin.*, 2023, **257**, 119697.

29 S. K. Gupta, K. Sudarshan and R. M. Kadam, *Mater. Lett.*, 2020, **279**, 128511.

30 M. Fakhrzad, A. H. Navidpour, M. Tahari and S. Abbasi, *Mater. Res. Express*, 2019, **6**, 095037.

31 T. Ivetić, in *Recent Advances in Porous Ceramics*, IntechOpen London, UK, 2018, pp. 80–81.

32 W. Guo, Y. Shuai, X. Liu, J. Zhang, J. Wang, K. H. Mahmoud, Z. M. El-Bahy and N. M. Mubarak, *Sens. Actuators, B*, 2022, **354**, 131221.

33 R. Malik, V. K. Tomer, V. Chaudhary, M. S. Dahiya, S. P. Nehra, P. S. Rana and S. Duhan, *Sens. Actuators, B*, 2017, **239**, 364–373.

34 M. Valdez, S. K. Gupta, K. Lozano and Y. Mao, *Sens. Actuators, B*, 2019, **297**, 126734.

35 Y. Zhao, L. Hu, H. Liu, M. Liao, X. Fang and L. Wu, *Sci. Rep.*, 2014, **4**, 6847.

36 S.-H. Wei and S. B. Zhang, *Phys. Rev. B: Condens. Matter Mater. Phys.*, 2001, **63**, 045112.

37 A. Lanje, S. Sharma, R. Pode and F. N. A. S. R. Ningthoujam, *Arch. Appl. Sci. Res.*, 2010, **2**, 127–135.

38 M. Dimitrievska, T. B. Ivetić, A. P. Litvinchuk, A. Fairbrother, B. B. Miljević, G. R. Štrbac, A. Pérez Rodríguez and S. R. Lukić-Petrović, *J. Phys. Chem. C*, 2016, **120**, 18887–18894.

39 J. Zeng, M. Xin, K. W. Li, H. Wang, H. Yan and W. Zhang, *J. Phys. Chem. C*, 2008, **112**, 4159–4167.

40 Q. Zhao, D. Ju, X. Song, X. Deng, M. Ding, X. Xu and H. Zeng, *Sens. Actuators, B*, 2016, **229**, 627–634.

41 S. Yuvaraj, W. J. Lee, C. W. Lee and R. K. Selvan, *RSC Adv.*, 2015, **5**, 67210–67219.

42 S. K. Gupta, B. Modak, D. Das, A. K. Yadav, P. Modak, A. K. Debnath and K. Sudarshan, *ACS Appl. Electron. Mater.*, 2021, **3**, 3256–3270.

43 Y. Yuan, K. Sheng, G. Zhuang, Q. Li, C. Dou, Q.-J. Fang, W.-W. Zhan, H. Gao, D. Sun and X. Han, *Chem. Commun.*, 2021, **57**, 8636–8639.

This journal is © the Owner Societies 2024

Phys. Chem. Chem. Phys., 2024, **26**, 7424–7434 | **7433**

44 S. K. Gupta, B. Modak, M. Tyagi, N. S. Rawat, P. Modak and K. Sudarshan, *ACS Omega*, 2022, **7**, 5311–5323.

45 Q. R. Hu, P. Jiang, H. Xu, Y. Zhang, S. L. Wang, X. Jia and W. H. Tang, *J. Alloys Compd.*, 2009, **484**, 25–27.

46 J. E. Montenegro, Y. Ochoa-Muñoz and J. E. Rodríguez-Páez, *Ceram. Int.*, 2020, **46**, 2016–2032.

47 J.-W. Zhao, L.-R. Qin and L.-D. Zhang, *Solid State Commun.*, 2007, **141**, 663–666.

48 A. Kolmakov and M. Moskovits, *Annu. Rev. Mater. Res.*, 2004, **34**, 151–180.

49 B. Bhagat, S. K. Gupta, D. Mandal, A. A. Gor, R. Bandyopadhyay and K. Mukherjee, *Chem. – Asian J.*, 2024, **19**, e202300841.

50 J. Rebholz, P. Bonanati, C. Jaeschke, M. Hübner, L. Mädler, U. Weimar and N. Barsan, *Sens. Actuators, B*, 2013, **188**, 631–636.

51 O. Lupan, D. Santos-Carballal, N. Magariu, A. K. Mishra, N. Ababii, H. Krüger, N. Wolff, A. Vahl, M. T. Bodduluri, N. Kohlmann, L. Kienle, R. Adelung, N. H. de Leeuw and S. Hansen, *ACS Appl. Mater. Interfaces*, 2022, **14**, 29331–29344.

52 S.-Y. Kim, J. Kim, W. H. Cheong, I. J. Lee, H. Lee, H.-G. Im, H. Kong, B.-S. Bae and J.-U. Park, *Sens. Actuators, B*, 2018, **259**, 825–832.

53 J. van den Broek, S. Abegg, S. E. Pratsinis and A. T. Güntner, *Nat. Commun.*, 2019, **10**, 4220.

54 N. Kotchasak, A. Wisitsoraat, A. Tuantranont, S. Phanichphant, V. Yordsri and C. Liewhiran, *Sens. Actuators, B*, 2018, **255**, 8–21.

55 R. Biswas and D. Saha, *Appl. Phys. A: Mater. Sci. Process.*, 2020, **126**, 313.

56 H. Liu, R. Wu, Q. Guo, Z. Hua and Y. Wu, *ACS Omega*, 2021, **6**, 30598–30606.

57 A. Nilabh, S. Sen, M. Narjinary and S. Kundu, *Microchem. J.*, 2020, **158**, 105146.

58 J.-Y. Kim, S. S. Kim and M. Tonezzer, *Sens. Actuators, B*, 2021, **335**, 129714.

59 S. K. Lalwani, A. Debnath and Sunny, *Nanotechnology*, 2022, **33**, 505502.

60 N. Banerjee and S. Roy, *Emerging Trends in Electronic Devices and Computational Techniques*, 2018, pp. 1–4.

61 H. R. Ansari, Z. Kordrostami and A. Mirzaei, *IEEE Trans. Instrum. Meas.*, 2023, **72**, 1–10.

62 K. Li, Y. Wu, M. Chen, Q. Rong, Z. Zhu, Q. Liu and J. Zhang, *Nanoscale Res. Lett.*, 2019, **14**, 57.

63 S. Singh and S. Sharma, *Sens. Actuators, B*, 2022, **350**, 130798.

64 Q. Hu, B. Huang, Y. Li, S. Zhang, Y. Zhang, X. Hua, G. Liu, B. Li, J. Zhou, E. Xie and Z. Zhang, *Sens. Actuators, B*, 2020, **307**, 127638.

65 Y. K. Moon, S.-Y. Jeong, Y. C. Kang and J.-H. Lee, *ACS Appl. Mater. Interfaces*, 2019, **11**, 32169–32177.

66 A. Dey, K. Kumari, A. Jana, B. Goswami, P. Nandi and S. K. Sarkar, Singapore, 2021.

67 Shailja, K. Singh, R. C. Singh and S. Sharma, *J. Phys.: Conf. Ser.*, 2021, **1849**, 012034.

68 J. Gu, B. Zhang, Y. Li, X. Xu, G. Sun, J. Cao and Y. Wang, *Sens. Actuators, B*, 2021, **343**, 130125.

69 D. An, Q. Wang, X. Tong, X. Lian, Y. Zou and Y. Li, *Ceram. Int.*, 2019, **45**, 6869–6874.

70 Z. Yao, X. Wang, M. Yang, H. Ma, Y. Sun, H. Zhang, T. Dong and W. Liu, *Semicond. Sci. Technol.*, 2020, **35**, 095030.

71 Y. Xu, L. Zheng, C. Yang, W. Zheng, X. Liu and J. Zhang, *Sens. Actuators, B*, 2020, **310**, 127846.

72 M. Poloju, N. Jayababu, E. V. Rao, R. G. Rao and M. V. R. Reddy, *Surf. Interfaces*, 2020, **20**, 100586.

73 G. Feng, Y. Che, C. Song, J. Xiao, X. Fan, S. Sun, G. Huang and Y. Ma, *Ceram. Int.*, 2021, **47**, 2471–2482.

74 L. Lv, P. Cheng, Y. Wang, L. Xu, B. Zhang, C. Lv, J. Ma and Y. Zhang, *Sens. Actuators, B*, 2020, **320**, 128384.

7434 | *Phys. Chem. Chem. Phys.*, 2024, **26**, 7424–7434

This journal is © the Owner Societies 2024